International Forum on Aeroelasticity and Structural Dynamics
IFASD 2019
9-13 June 2019 Savannah, Georgia, USA

INCLUDING GEOMETRICALLY NONLINEAR FLUTTER CONSTRAINTS IN HIGH FIDELITY AIRCRAFT OPTIMIZATION

Christopher A. Lupp[1], Carlos E.S. Cesnik[1], Philip Beran[2], Joshua Deaton[2], David Easterling[2]

[1]University of Michigan, Department of Aerospace Engineering

[2]Air Force Research Laboratory, Wright-Patterson Air Force Base, Dayton, OH

Abstract: Higher aspect ratio, more flexible wings pose an aeroelastic design challenge for future aircraft. These vehicles may encounter geometrically nonlinear effects and/or participation of rigid body degrees of freedom in their flutter modes. If geometrically nonlinear flutter analyses are not included during the design process, the final configuration obtained may be infeasible. This paper presents the inclusion of a beam-based nonlinear flutter constraint in a multi-fidelity aircraft optimization framework in which the objective function is evaluated using high-fidelity FEM simulations. The flutter constraint is applied to the entire flight envelope thereby ensuring a feasible design. The beam-based constraint is coupled with the high-fidelity optimization problem using an equivalent beam condensation process. The gradients of the condensation process are evaluated and verified. Finally, the assembled multi-fidelity problem is evaluated for the initial optimization iteration.

NOMENCLATURE

AD	Algorithmic Differentiation
BWB	blended wing body
FEM	finite element method
KS	Kreisselmeier-Steinhauser
MDO	multidisciplinary design optimization
RBe	rigid body element
uCRM	undeformed Common Research Model
UM/NAST	University of Michigan's Nonlinear Aeroelastic Simulation Toolbox

1 METHODOLOGY AND NUMERICAL METHODS

The multi-fidelity problem is defined in OpenMDAO and uses a high-fidelity solution to obtain the objective function and high-fidelity constraints (such as a stress constraint). While these offer valuable information for structural sizing, the computational expense of determining dynamic aeroelastic constraints using the high-fidelity solution is prohibitive for optimization

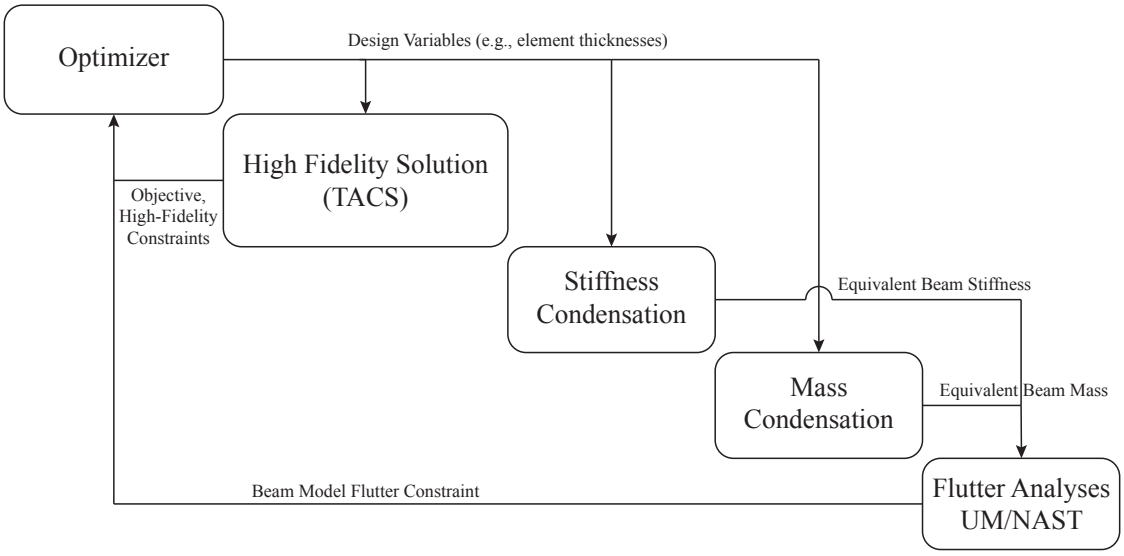

Figure 1: Diagram of the multi-fidelity optimization problem. The objective function and high-fidelity constraints are evaluated by the high-fidelity solution, while the flutter constraint is evaluated by the beam model.

problems, especially when geometrical nonlinearities must be considered. As such, the flutter constraint is evaluated using a geometrically nonlinear beam model (Figure 1). Beam properties for beam model are determined using an equivalent beam condensation [1], which has been previously used to enable nonlinear aeroelastic analyses of transport aircraft [2]. Derivatives for the gradient-based optimization are determined on the component level and the global Jacobian is assembled automatically by OpenMDAO.

1.1 OpenMDAO

OpenMDAO [3] is an open source software framework designed to enable Multidisciplinary Design Analysis and Optimization (MDAO), using gradient-based optimization. The framework was written in Python and allows the integration of external software, e.g., C++ programs using Cython. An OpenMDAO problem consists of *Components* that are assembled together to define the global problem. This modular approach simplifies evaluating the problem gradients to defining the gradient at the Component level, providing derivatives for the Component outputs with respect to its inputs. OpenMDAO uses the partials defined in this manner to assemble the global Jacobians while utilizing problem sparsity for computational efficiency. Within this work, we employ OpenMDAO as the coupling agent between the individual disciplines (each box in Figure 1), taking advantage of the behind-the-scenes assembly of the global sensitivities.

1.2 TACS

The high-fidelity objective function of the multi-fidelity problem is defined and solved using the TACS FEM code [4]. TACS uses MPI for parallel solution evaluations and has the ability to provide an adjoint-based gradient for gradient-based optimization. It has been used for shell-based optimization problems and topology optimization using solid elements. As such, TACS is well suited for the proposed multi-fidelity problem.

1.3 UM/NAST

The University of Michigan's Nonlinear Aeroelastic Simulation Toolbox (UM/NAST) [5–7] is a framework to model coupled nonlinear aeroelastic and flight mechanics behavior of very flex-

ible aircraft. It uses a strain-based, geometrically nonlinear beam formulation to solve structural dynamic and aeroelastic problems and is capable of modeling slender, very flexible structures accurately. Multiple aerodynamic models are available including strip theory with Peter's finite state aerodynamics [8], method of segments [9], and UVLM with propeller effects [10, 11]. Furthermore, the code is able to determine coupled nonlinear sensitivities [12] and can interface with the Python-based OpenMDAO using a Cython wrapper.

1.4 Flutter Constraint

Jonsson et al. [13] provides a detailed discussion on different flutter constraint methodologies. The flutter constraint used in this work was developed in [12]. The flutter damping values of the aircraft for various flight conditions are constrained such that no instabilities occur. However, to obtain a scalar flutter constraint, a double aggregation with Kreisselmeier-Steinhauser (KS) functions is used, as proposed by Jonsson and Martins [14]:

$$KS\left(KS\left(\mathrm{Re}\left(\lambda_i\right)\right)\right) \leq 0 \tag{1}$$

As geometrically nonlinear flutter problems can depend on a large number of variables (angle of attack, control surface deflections, etc.), an accurate flutter constraint is highly dependent on how the flight envelope was sampled. Details on sampling strategies applied to the flutter constraint—and potential pitfalls—have been investigated by Lupp and Cesnik [12].

2 EQUIVALENT BEAM CONDENSATION PROCESS

The beam condensation consists of two separate processes: a mass condensation and a stiffness condensation. The mass condensation simplifies every element as a point mass and determines the equivalent beam mass properties from these. The equivalent beam stiffness properties are determined from FEM runs for linearly independent load cases. Gradients for the mass condensation are determined analytically, while the stiffness sensitivities are determined using Algorithmic Differentiation (AD).

2.1 Mass Condensation

The mass condensation uses the high-fidelity FEM model and reduces it to point masses—one for every element (Figure 2). For an entire model, the high fidelity model must be subdivided such that every beam node is associated with its neighboring high fidelity elements. This can be achieved, for example, using a nearest neighbor approach. The mass of every element is determined from the element area and density, assuming a constant element thickness:

$$m_j = \rho A t \tag{2}$$

The element area is determined from the element corner points using Heron's formula (using two triangles for quadrilateral elements).The equivalent beam mass is then obtained from the sum of the element masses associated with the beam section.

$$m_e = \sum_{j=1}^{N} m_j \tag{3}$$

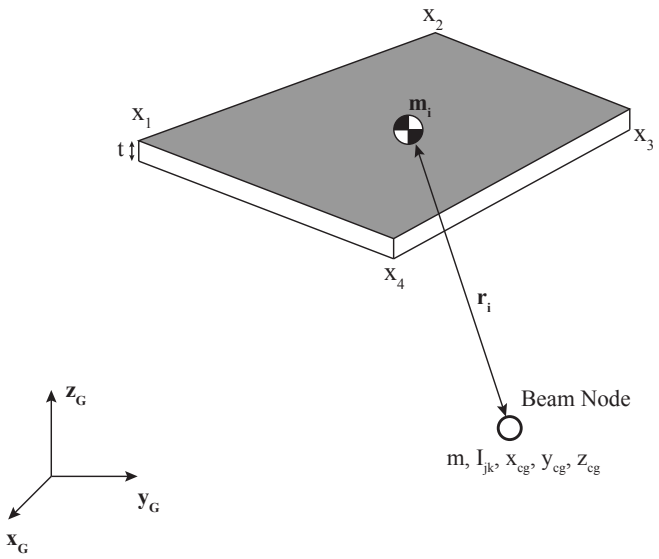

Figure 2: Relationship between a mass element and the beam reference node.

The center of gravity of the beam section (determined from the individual element masses) is:

$$x_{cg} = \frac{\sum_{j=1}^{N} m_j r_{xj}}{\sum_{j=1}^{N} m_j} \tag{4}$$

$$y_{cg} = \frac{\sum_{j=1}^{N} m_j r_{yj}}{\sum_{j=1}^{N} m_j} \tag{5}$$

$$z_{cg} = \frac{\sum_{j=1}^{N} m_j r_{zj}}{\sum_{j=1}^{N} m_j} \tag{6}$$

Finally, the inertia of the equivalent beam section (determined from the individual element masses) is:

$$I_{xx} = \sum_{j=1}^{N} m_j \left(r_{yj}^2 + r_{zj}^2 \right) \tag{7}$$

$$I_{xy} = \sum_{j=1}^{N} m_j r_{xj} r_{yj} \tag{8}$$

$$I_{xz} = \sum_{j=1}^{N} m_j r_{xj} r_{zj} \tag{9}$$

$$\tag{10}$$

$$I_{yy} = \sum_{j=1}^{N} m_j \left(r_{xj}^2 + r_{zj}^2 \right) \tag{11}$$

$$I_{yz} = \sum_{j=1}^{N} m_j r_{yj} r_{zj} \tag{12}$$

$$I_{zz} = \sum_{j=1}^{N} m_j \left(r_{xj}^2 + r_{yj}^2 \right) \tag{13}$$

2.2 Mass Condensation Gradients

Because the beam condensation is applied to a gradient-based optimization problem, efficiently and accurately determining the gradients is paramount. As mentioned previously, the determination of the gradients is subdivided on the component level of the optimization problem. As such, the gradients of the mass properties with respect to the component design variables (element thicknesses and densities) are required. The formulae for the mass condensation process are comparatively simple, so the gradients were obtained analytically. The derivatives of the beam section mass w.r.t. element thickness element density are:

$$\frac{\partial m}{\partial t_i} = \sum_{j=1}^{N} \frac{\partial m_j}{\partial t_i} = \frac{\partial m_i}{\partial t_i} \tag{14}$$

$$\frac{\partial m}{\partial \rho_i} = \sum_{j=1}^{N} \frac{\partial m_j}{\partial \rho_i} = \frac{\partial m_i}{\partial \rho_i} \tag{15}$$

It is worth noting that the gradients simplify to the derivative of the mass element w.r.t. its inputs, with all other entries of the gradient vector equaling zero. This simplifies the derivatives of the other mass properties and also results in a sparse Jacobian, which improves computational efficiency.

The derivatives of the center of gravity are determined using the quotient rule:

$$\frac{\partial x_{cg}}{\partial t_i} = \frac{\frac{\partial m_i}{\partial t_i} r_{xi} \sum_{j=1}^{N} m_j - \frac{\partial m_i}{\partial t_i} \sum_{j=1}^{N} m_j r_{xj}}{\left(\sum_{j=1}^{N} m_j \right)^2} \tag{16}$$

The element mass the equation for the center of gravity can be rearranged to obtain:

$$\sum_{j=1}^{N} m_j r_{xj} = x_{cg} \sum_{j=1}^{N} m_j \tag{17}$$

Using the Equation 17, the center of gravity gradients w.r.t. element thickness and density simplify to:

$$\frac{\partial x_{cg}}{\partial t} = \frac{\frac{\partial m_i}{\partial t_i} (r_{xi} - x_{cg})}{m_e} \tag{18}$$

$$\frac{\partial y_{cg}}{\partial t} = \frac{\frac{\partial m_i}{\partial t_i} (r_{yi} - y_{cg})}{m_e} \tag{19}$$

$$\frac{\partial z_{cg}}{\partial t} = \frac{\frac{\partial m_i}{\partial t_i} (r_{zi} - z_{cg})}{m_e} \tag{20}$$

$$\frac{\partial x_{cg}}{\partial \rho_i} = \frac{\frac{\partial m_i}{\partial \rho_i} (r_{xi} - x_{cg})}{m_e} \tag{21}$$

$$\frac{\partial y_{cg}}{\partial \rho_i} = \frac{\frac{\partial m_i}{\partial \rho_i} (r_{yi} - y_{cg})}{m_e} \tag{22}$$

$$\frac{\partial z_{cg}}{\partial \rho_i} = \frac{\frac{\partial m_i}{\partial \rho_i} (r_{zi} - z_{cg})}{m_e} \tag{23}$$

Finally, the derivatives of the inertia of the beam section w.r.t. the element thickness and density are:

$$\frac{\partial I_{xx}}{\partial t_i} = \frac{\partial m_i}{\partial t_i}\left(r_{yj}^2 + r_{zj}^2\right) \tag{24}$$
$$\frac{\partial I_{xy}}{\partial t_i} = \frac{\partial m_i}{\partial t_i} r_{xj} r_{yj} \tag{25}$$
$$\frac{\partial I_{xz}}{\partial t_i} = \frac{\partial m_i}{\partial t_i} r_{xj} r_{zj} \tag{26}$$
$$\frac{\partial I_{yy}}{\partial t_i} = \frac{\partial m_i}{\partial t_i}\left(r_{xj}^2 + r_{zj}^2\right) \tag{27}$$
$$\frac{\partial I_{yz}}{\partial t_i} = \frac{\partial m_i}{\partial t_i} r_{yj} r_{zj} \tag{28}$$
$$\frac{\partial I_{zz}}{\partial t_i} = \frac{\partial m_i}{\partial t_i}\left(r_{xj}^2 + r_{yj}^2\right) \tag{29}$$

$$\frac{\partial I_{xx}}{\partial \rho_i} = \frac{\partial m_i}{\partial \rho_i}\left(r_{yj}^2 + r_{zj}^2\right) \tag{30}$$
$$\frac{\partial I_{xy}}{\partial \rho_i} = \frac{\partial m_i}{\partial \rho_i} r_{xj} r_{zj} \tag{31}$$
$$\frac{\partial I_{xz}}{\partial \rho_i} = \frac{\partial m_i}{\partial \rho_i} r_{xj} r_{zj} \tag{32}$$
$$\frac{\partial I_{yy}}{\partial \rho_i} = \frac{\partial m_i}{\partial \rho_i}\left(r_{xj}^2 + r_{zj}^2\right) \tag{33}$$
$$\frac{\partial I_{yz}}{\partial \rho_i} = \frac{\partial m_i}{\partial \rho_i} r_{yj} + r_{zj} \tag{34}$$
$$\frac{\partial I_{zz}}{\partial \rho_i} = \frac{\partial m_i}{\partial \rho_i}\left(r_{xj}^2 + r_{yj}^2\right) \tag{35}$$

2.3 Stiffness Condensation

The equivalent beam stiffness condensation used in this work was first proposed by Malcolm and Laird [1] to accurately deduce beam properties of wind turbine blades for subsequent aeroelastic analyses. The process has since been applied to aircraft structures [15, 16]. Furthermore, Stodieck et al. [16] extended the Malcolm's process to obtain gradients of the stiffness properties for equivalent beam condensations in optimization problems.

The stiffness condensation component within this work consists of two distinct processes (Figure 3): high-fidelity FEM runs to obtain equivalent beam displacements and the determination of the stiffness properties (from the equivalent beam displacements previously determined).

The high-fidelity FEM simulations are conducted for six linearly independent load cases to obtains six sets of beam displacements. In this work, these load cases are evaluated using Nastran and the equivalent beam displacements recovered using rigid body elements (RBEs). A set of six linearly independent load cases are:

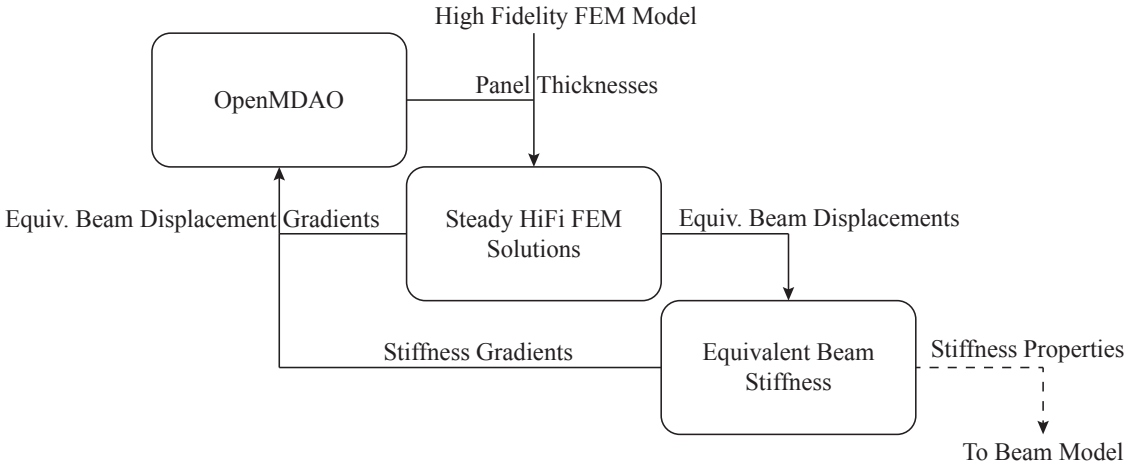

Figure 3: Block diagram of the complete stiffness condensation process including high-fidelity FEM solutions and the ensuing determination of equivalent beam stiffnesses.

$$\left(F^t\right)_1 = \left\{ \begin{array}{cccccc} F_x & 0 & 0 & 0 & 0 & 0 \end{array} \right\}^T \tag{36}$$

$$\left(F^t\right)_2 = \left\{ \begin{array}{cccccc} 0 & F_y & 0 & 0 & 0 & 0 \end{array} \right\}^T \tag{37}$$

$$\left(F^t\right)_3 = \left\{ \begin{array}{cccccc} 0 & 0 & F_z & 0 & 0 & 0 \end{array} \right\}^T \tag{38}$$

$$\left(F^t\right)_4 = \left\{ \begin{array}{cccccc} 0 & 0 & 0 & M_x & 0 & 0 \end{array} \right\}^T \tag{39}$$

$$\left(F^t\right)_5 = \left\{ \begin{array}{cccccc} 0 & 0 & 0 & 0 & M_y & 0 \end{array} \right\}^T \tag{40}$$

$$\left(F^t\right)_6 = \left\{ \begin{array}{cccccc} 0 & 0 & 0 & 0 & 0 & M_z \end{array} \right\}^T \tag{41}$$

The element stiffness matrix is evaluated from the internal forces f^i, which result from the applied tip loads (Figure 4), and the element strains:

$$f^i = \left\{ \begin{array}{c} f_x^i \\ f_y^i \\ f_z^i \\ m_x^i \\ m_y^i \\ m_z^i \end{array} \right\} = [k] \{\varepsilon\} \tag{42}$$

The element strains are defined in Equation 43 and can be rewritten in terms of displacements:

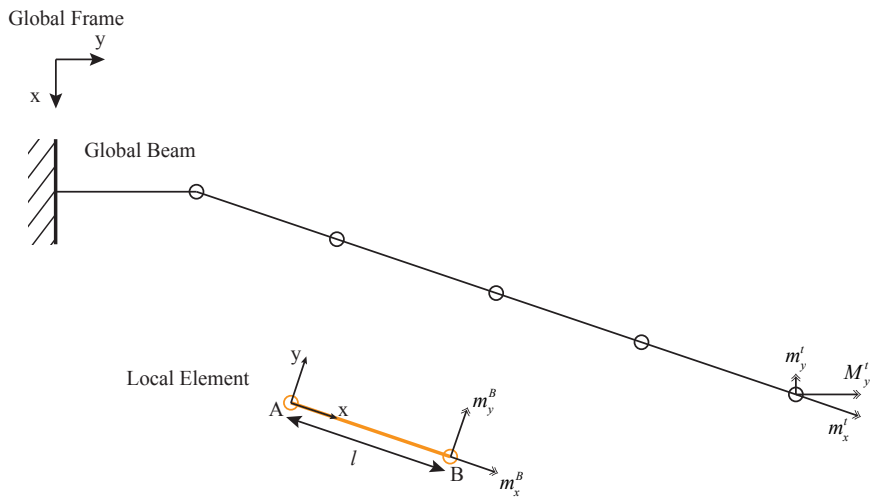

Figure 4: Diagram of the coordinate frames and global and local load conventions (shown here for an applied tip moment) of the stiffness condensation process.

$$\varepsilon = \begin{Bmatrix} \varepsilon_x \\ \gamma_y \\ \gamma_z \\ \kappa_x \\ \kappa_y \\ \kappa_z \end{Bmatrix} \tag{43}$$

$$= \begin{Bmatrix} \frac{\partial u_x}{\partial x} \\ \frac{\partial u_y}{\partial x} \\ \frac{\partial u_z}{\partial x} \\ \frac{\partial \theta_x}{\partial x} \\ \frac{\partial \theta_y}{\partial x} \\ \frac{\partial \theta_z}{\partial x} \end{Bmatrix} + \begin{Bmatrix} 0 \\ -\theta_z \\ \theta_y \\ 0 \\ 0 \\ 0 \end{Bmatrix} \tag{44}$$

$$= \begin{Bmatrix} \frac{\partial u_x}{\partial x} \\ \frac{\partial u_y}{\partial x} \\ \frac{\partial u_z}{\partial x} \\ \frac{\partial \theta_x}{\partial x} \\ \frac{\partial \theta_y}{\partial x} \\ \frac{\partial \theta_z}{\partial x} \end{Bmatrix} + \int_0^x \begin{Bmatrix} 0 \\ -\kappa_z \\ \kappa_y \\ 0 \\ 0 \\ 0 \end{Bmatrix} \mathrm{dx} \tag{45}$$

The element local displacement and local internal force vectors u and f are obtained by transforming the global displacements U and F in to the local coordinate system:

$$u = \begin{Bmatrix} u_x \\ u_y \\ u_z \\ \theta_x \\ \theta_y \\ \theta_z \end{Bmatrix} = [T] \{U\} \tag{46}$$

$$f^t = [T]\, F^t \tag{47}$$

The element stiffness properties are determined by initially solving for the stiffness matrix in the local frame. The local element stiffness matrix is obtained from:

$$f^i = [K]\, \{\Delta u\} \tag{48}$$

with

$$\{\Delta u\} = \left\{ \begin{array}{c} u_x^B - u_x^A \\ u_y^B - u_y^A - l\theta_z^A \\ u_z^B - u_z^A + l\theta_y^A \\ \theta_x^B - \theta_x^A \\ \theta_y^B - \theta_y^A \\ \theta_z^B - \theta_z^A \end{array} \right\} = [k]\, \{\varepsilon\} \tag{49}$$

Malcolm [1] derived the relationship between the local stiffness matrix K and the stiffness matrix k in Lyapunov form, which can be solved for k^{-1} using Lyapunov's method:

$$K^{-1}Q^{-1} = k^{-1}HQ^{-1} + Ek^{-1} \tag{50}$$

with

$$E = \begin{bmatrix} 0 & 0 & 0 & 0 & 0 & 0 \\ 0 & 0 & 0 & 0 & 0 & 1 \\ 0 & 0 & 0 & 0 & -1 & 0 \\ 0 & 0 & 0 & 0 & 0 & 0 \\ 0 & 0 & 0 & 0 & 0 & 0 \\ 0 & 0 & 0 & 0 & 0 & 0 \end{bmatrix} \tag{51}$$

$$H = \begin{bmatrix} l & 0 & 0 & 0 & 0 & 0 \\ 0 & l & 0 & 0 & 0 & 0 \\ 0 & 0 & l & 0 & 0 & 0 \\ 0 & 0 & 0 & l & 0 & 0 \\ 0 & 0 & -\frac{l^2}{2} & 0 & l & 0 \\ 0 & \frac{l^2}{2} & 0 & 0 & 0 & l \end{bmatrix} \tag{52}$$

$$Q = \begin{bmatrix} \frac{l^2}{2} & 0 & 0 & 0 & 0 & 0 \\ 0 & \frac{l^2}{2} & 0 & 0 & 0 & 0 \\ 0 & 0 & \frac{l^2}{2} & 0 & 0 & 0 \\ 0 & 0 & 0 & \frac{l^2}{2} & 0 & 0 \\ 0 & 0 & -\frac{l^3}{3} & 0 & \frac{l^2}{2} & 0 \\ 0 & \frac{l^3}{3} & 0 & 0 & 0 & \frac{l^2}{2} \end{bmatrix} \tag{53}$$

2.4 Stiffness Condensation Gradients

As with the equivalent beam mass condensation, the gradients of the stiffness condensation with respect to its input variables are required for the optimization problem (Figure 3). While the mass condensation gradients were determined analytically, the gradients of the stiffness condensation component were determined using AD, while the gradients of the FEM solutions needed for the condensation are obtained from the FEM solution itself. For this work Nastran's SOL 200 was used for this purpose. Based on previous studies of AD libraries [12], the C++ library CoDiPack [17] was chosen.

The stiffness condensation in this work was implemented using templates, permitting the function evaluation using standard C++ floating precision types without the overhead of operator overloading AD. The evaluation of the gradient with respect to the equivalent beam displacements is then evaluated using the CoDiPack types. It should be noted, that the stiffness matrix of a given element only depends on the displacements of that element's corner nodes and is independent of any other nodes' displacements. As a result, the Jacobian of the stiffness properties is very sparse, yielding a more computationally efficient solution.

3 NUMERICAL STUDIES

Now that the beam condensation process and the formulation of its derivatives have been introduced, the mass and stiffness condensation components must be verified. The mass condensation is tested using a simple plate example, for which analytical mass properties are obtained, while the stiffness condensation is tested and compared to a simple beam model with known stiffness properties. The gradients of both the mass and stiffness condensation processes are verified against reference results obtained using the complex step method. The verification of the individual components in this manner offers confidence in the accuracy of the assembled problem, as the assembly of the global Jacobian is conducted by OpenMDAO. This equates to the application of the chain rule using verified derivatives and as such, the global gradients will be accurate as long as the component gradients have been verified.

After verifying the component gradients, an assembled optimization problem (mass minimization) is investigated using a very flexible transport aircraft configuration. The objective function and constraint values are reported for the first optimization iteration along with the global gradients of the flutter constraint with respect to a subset of the design variables.

Mass Condensation

The mass condensation component is verified using a simple plate configuration (Figure 5). The plate properties are listed in Table 1. The component results are compared to analytical values for mass, inertia, and center of gravity position (Table 1). The values obtained from the mass condensation match the analytical values to machine precision.

Next, the accuracy of the gradient values obtained by the mass condensation component are quantified. To this end, a single mass element of the plate is perturbed using an imaginary disturbance ih. The gradient reference gradient is then determined using the complex step method:

$$g\left(x\right) \approx \frac{Im\left(f\left[x+ih\right)\right]}{h} \tag{54}$$

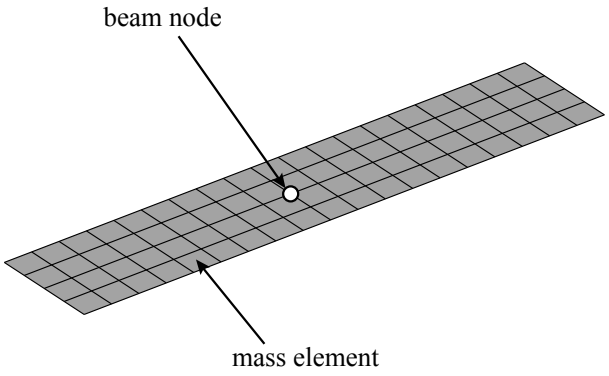

Figure 5: Plate example for testing the mass condensation process and verification of mass condensation gradients.

Table 1: Plate properties of the verification test case as well as component and analytical reference results for the mass condensation.

	Value	Reference Value
Plate Length, m	1.0	–
Plate Width, m	0.2	–
Plate Thickness, m	0.01	–
Plate Density, kg/m^3	2700.0	–
Verification Results		
Mass, kg	5.39999999999999	5.4
x_{cg}, m	0.10000000000000006	0.1
y_{cg}, m	0.5000000000000003	0.5
z_{cg}, m	0.0	0.0

Because the step size h is chosen at machine precision (10^{-16}), the derivative obtained using the complex step method is accurate to machine precision. The gradient results from the mass component and the corresponding reference results are listed in Table 2. The gradient obtained from the mass condensation component matches the complex step results to machine precision. As a result, the mass property gradients are accurate to machine precision.

Stiffness Condensation

Similar to the mass condensation component, the stiffness condensation component must be verified before use in the assembled problem. A simple beam configuration is used as a test case. The stiffness condensation component then utilizes the beam displacements to determine the equivalent beam stiffness properties. As the source data is obtained from a beam, reference stiffness data is available for comparison. The stiffness property gradients are verified similar to the mass condensation. An imaginary perturbation to the displacments of a beam node are applied and the reference derivatives are determined using complex step (Figure 6).

Equation 55 shows the result from the stiffness property verification. Clearly, the stiffness property function values, while less accurate than the mass condensation, are sufficiently accurate for the multi-fidelity problem. The stiffness property gradients, on the other hand are accurate

Table 2: Comparison of the mass condensation component gradients with respect to mass element thickness with reference results using the complex step method.

	Component	Complex Step
$\frac{\partial m}{\partial t}$	7.105263157894723	7.105263157894723
$\frac{\partial I_{xx}}{\partial t}$	3.07533897069543	3.07533897069543
$\frac{\partial I_{yy}}{\partial t}$	0.039967105263157825	0.039967105263157825
$\frac{\partial I_{zz}}{\partial t}$	3.1153060759585878	3.1153060759585878
$\frac{\partial x_{cg}}{\partial t}$	-0.03289473684210529	-0.03289473684210529
$\frac{\partial y_{cg}}{\partial t}$	0.20775623268697985	0.20775623268697985
$\frac{\partial z_{cg}}{\partial t}$	0.0	0.0

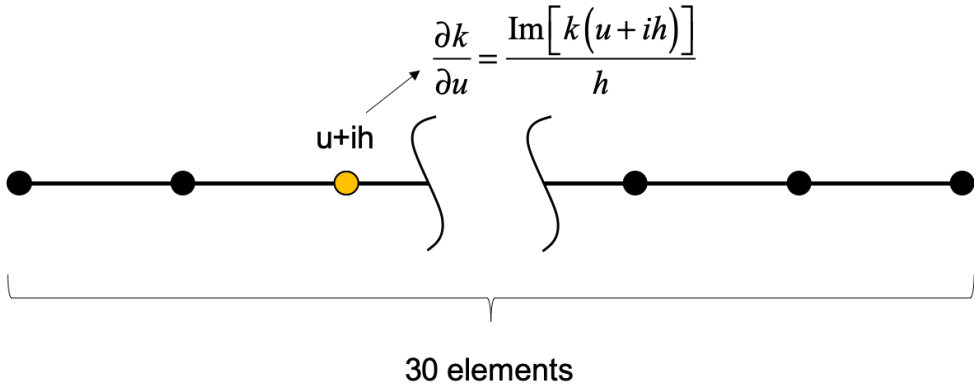

Figure 6: Stiffness condensation verification test case.

to machine precision compared to the reference data. This is because the AD method used to determine the component derivatives is accurate to machine precision (w.r.t. its inputs, the beam displacements). The discrepancy in accuracy between the function and gradient values can be explained that the function value is being compared to an external reference value. The gradient, by contrast, is compared to a reference value which depends on the function input variables. This explains the close correlation between the gradient values despite the larger difference in the function value.

$$k_1^{NAST} = \begin{bmatrix} 1.2615 \times 10^9 & 1.8566 \times 10^{-5} & -0.0866 & 3.1114 \\ 1.8566 \times 10^{-5} & 9.6953 \times 10^6 & -0.4323 & 0.0194 \\ -0.0866 & -0.4323 & 7.5533 \times 10^6 & 1.6162 \times 10^{-3} \\ 3.1114 & 0.0194 & 1.6162 \times 10^{-3} & 121.7089 \times 10^6 \end{bmatrix} \tag{55}$$

$$\left(\frac{\partial K_{22}}{\partial t}\right)_{component} = 6.28593421152476 \times 10^{-4} \tag{56}$$

$$\left(\frac{\partial K_{22}}{\partial t}\right)_{reference} = 6.28593421152476 \times 10^{-4} \tag{57}$$

3.1 uCRM 13.5 Configuration

The undeformed Common Research Model (uCRM) 13.5 (Figure 7) configuration is a very flexible transport aircraft configuration designed by the MDO Lab at the University of Michigan

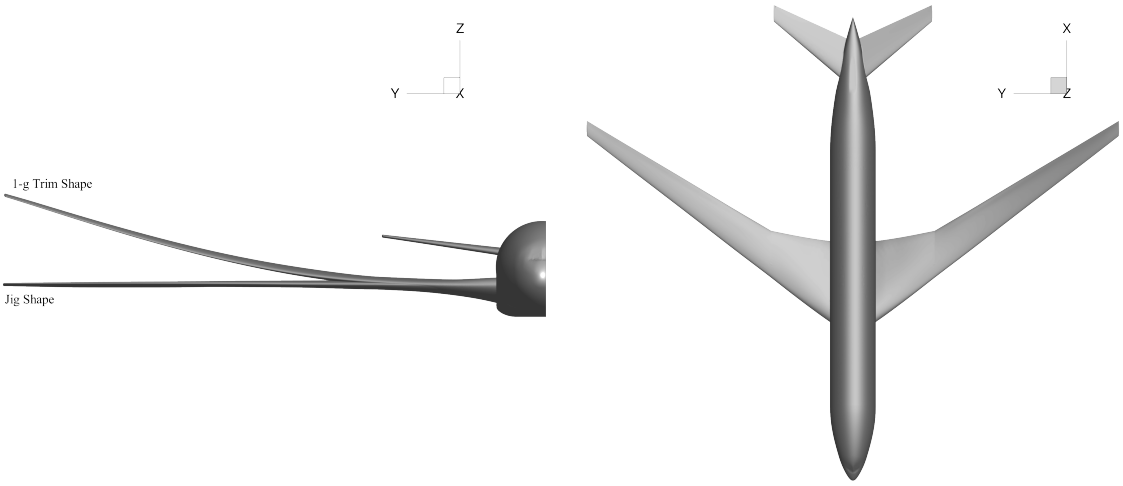

Figure 7: Two side view of the uCRM 13.5 showing the planform, jig shape and 1-g trim shape.

[18]. The model was designed using high-fidelity optimization without a flutter constraint and experiences large deformations. Therefore, it offers a compelling case study for applying the geometrically nonlinear flutter constraint within the multi-fidelity optimization problem. The original uCRM configuration contained orthotropic elements to model stiffeners. To simplify the optimization problem, the wing skins were modeled as isotropic material.

A UM/NAST beam model of the uCRM wing was created. The beam nodes were placed at the rib locations, at the center of the wing box so that the beam reference axis remains close to the wing shear axis (Figure 8). Aerodynamics are modeled using strip theory with Peters' finite state aerodynamics.

3.2 Assembled Multi-Fidelity Problem

After having verified the individual components of the multi-fidelity problem, the entire optimization problem is assembled. The multi-fidelity optimization problem is formulated as a mass minimization with respect to wing skin thicknesses and subject to stress constraints from high fidelity FEM solutions. Additionally, a lower fidelity flutter constraint is imposed, such that no flutter occurs within the flight envelope, as previously described. Instead of a high-fidelity aerostructural solution, a uniform load is applied across the span. The block diagram of the optimization process is shown in Figure 1. The optimization problem is formulated as:

$$
\begin{aligned}
&\text{minimize:} && m_{struc} \\
&\text{with respect to:} && \mathrm{x} = \left[t_i\right]^T \\
&\text{subject to:} && \\
& && KS\left(\sigma_{Mises}\right) \leq \sigma_{yield} \\
& && KS\left(KS\left(\lambda_i\right)\right) \leq 0
\end{aligned}
\tag{58}
$$

A single optimization iteration is conducted and the resulting function and gradient values reported. Additionally, a runtime comparison between the objective function and flutter constraint evaluation conducted. While this is not an equal comparison—the objective function consists of

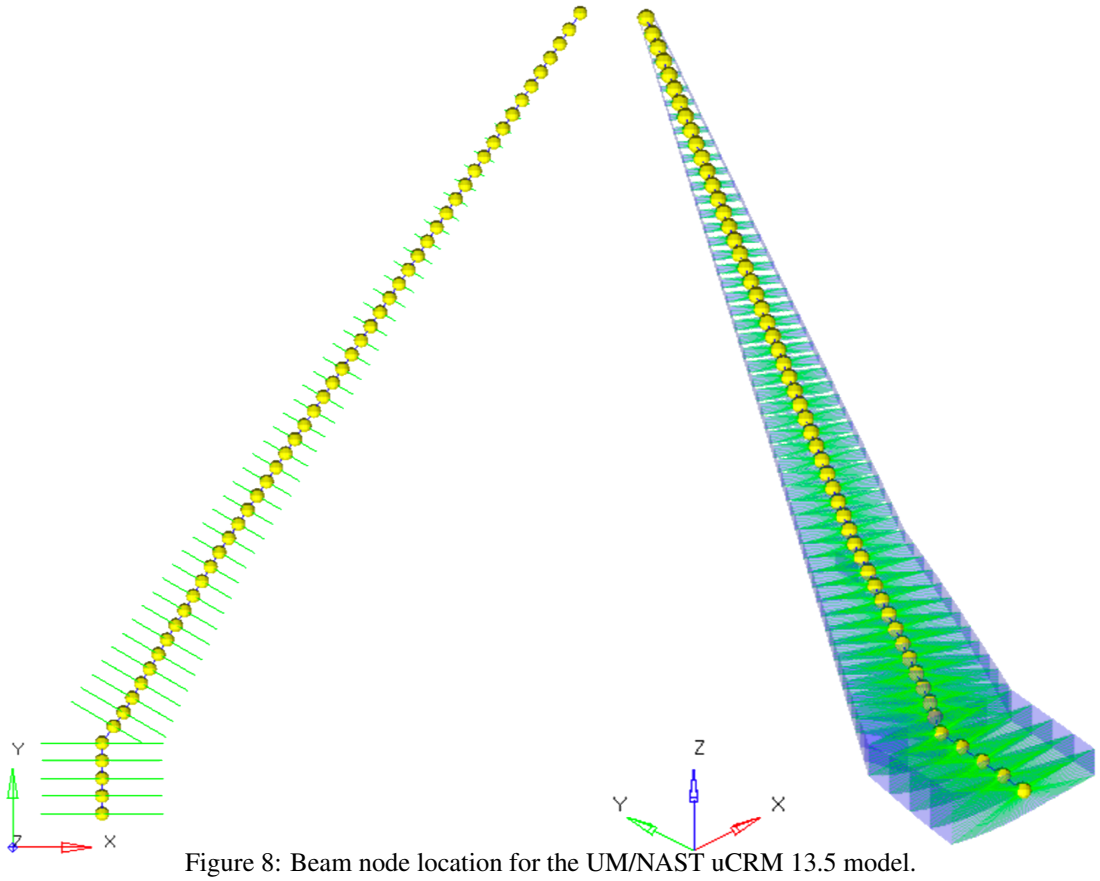

Figure 8: Beam node location for the UM/NAST uCRM 13.5 model.

linear static simulation that is faster than a nonlinear high-fidelity flutter solution–it does serve as a lower bound of the possible speedup when using the multi-fidelity approach.

Single Optimization Iteration

A single optimization iteration is evaluated to illustrate the interaction of the individual components in the multi-fidelity problem. Figure 9 shows the wing loading and deformation for the first optimization iteration. The objective function values and global gradient of the flutter constraint are listed in Table 3.

Runtime Comparison

The ability to save wall time during the flutter constraint evaluation poses a potentially significant advantage of the multi-fidelity problem over an optimization problem evaluated solely

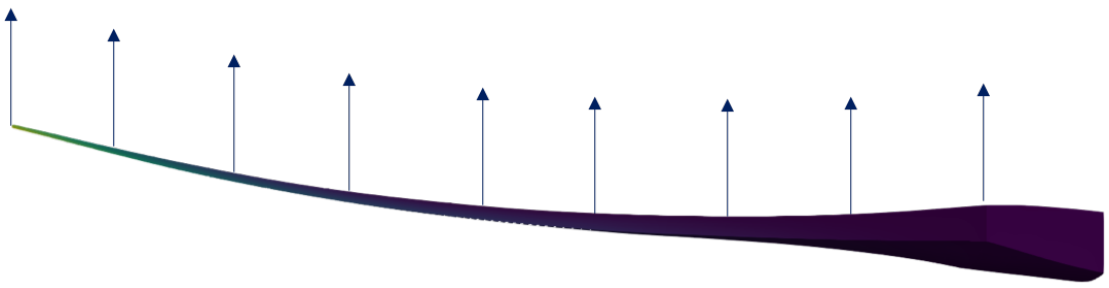

Figure 9: Bending deformation of the uCRM wing box for the initial iteration.

Table 3: Solution values for the first optimization iteration.

	Value
Wing Mass, kg	17446.4035
Stress Constraint	0.997823861
Flutter Constraint	0.57
Flutter Constraint Gradient	0.00004513

Table 4: Comparison of the wall time required for an objective function evaluation and for the evaluation of the flutter constraint.

	Wall Time, s
Objective	38.6
Flutter Constraint	18.2

using high-fidelity methods. To quantify this, the wall time of the objective function was captured without further condensation processes or constraints. Next, the condensation processes and the flutter constraint were evaluated without the high-fidelity objective function or high-fidelity constraints. Obviously, the constraints and objective function are evaluated together at every optimization iteration. However, seperating out the respective evaluations is necessary to obtain accurate wall time results. A series of ten evaluations were run and the times averaged (Table 4).

The high-fidelity objective function evaluation requires more than twice the wall time as the flutter constraint evaluation (incl. the condensation processes). While adding additional flutter search points and evaluating them in series would result in additional wall time, the parallel evaluation of the search points would result in a similar wall time to the one reported here (provided there are enough CPU threads available). Furthermore, it is noteworthy that this comparison truly is a lower bound of the speedup obtained by using a lower-fidelity flutter constraint. The static solution used in the objective function is linear and computationally cheaper than evaluating a nonlinear flutter constraint.

4 CONCLUDING REMARKS

This paper presented a multi-fidelity approach to including nonlinear flutter constraints into high-fidelity MDO problems. Equivalent beam mass and stiffness condensation processes were developed from previously existing work and the derivatives for these components were obtained. The gradients determined within the equivalent beam condensation processes are highly sparse, resulting in reduced computational expense. The function and gradient values of the condensation processes were verified and the gradient data was shown to be accurate to machine precision. After verifying the equivalent beam condensation process, the assembled problem was investigated. A single optimization iteration was conducted and the global gradient data was reported. Finally, the run time of the low-fidelity constraint was compared to the high fidelity solution to quantify the computational advantage of the multi-fidelity approach.

However, including flutter constraints, even linear ones, poses computational challenges. Including a flutter constraint which accounts for geometrically nonlinear effects further increases the computational cost significantly. As such, multi-fidelity problems in which the geometrically nonlinear flutter problem is accounted for using a lower-fidelity model may turn a compu-

tationally infeasible problem into a feasible one. Moreover, as the flutter constraint presented here requires less wall time than the objective function evaluation, it is conceivable that the flutter constraint could be evaluated in parallel to the objective function (provided sufficient CPU threads). As a result, it is possible to include geometrically nonlinear flutter constraints into high-fidelity MDO problems at similar computational cost to existing high-fidelity steady problems.

ACKNOWLEDGEMENTS

The authors would like to thank Divya Sanghi for discussion about the stiffness condensation process and for providing reference data for the function value verification. This work is supported by the U.S. Air Force Research Laboratory (AFRL) under the Michigan-AFRL Collaborative Center in Aerospace Vehicle Design (CCAVD), with Dr. Philip Beran as the task Technical Monitor. Opinions, interpretations, conclusions, and recommendations are those of the authors and are not necessarily endorsed by the United States Government. Cleared for public release, distribution unlimited (88ABW-2019-2410).

5 REFERENCES

[1] Malcolm, D. J. and Laird, D. L. (2007). Extraction of Equivalent Beam Properties from Blade Models. *Wind Energy*, 10, 135–157.

[2] Kitson, R., Lupp, C. A., and Cesnik, C. E. S. (2016). Modeling and simulation of flexible jet transport aircraft with high-aspect-ratio wings. In *15th Dynamics Specialists Conference*. San Diego, CA: AIAA. ISBN 9781624103988.

[3] Gray, J. S., Hwang, J. T., Martins, J. R. R. A., et al. (2019). OpenMDAO : An open-source framework for multidisciplinary design , analysis , and optimization. *Structural and Multidisciplinary Optimization*, 59(4), 1—-39. doi:10.1007/s00158-019-02211-z.

[4] Kennedy, G. J. and Martins, J. R. R. A. (2014). A parallel finite-element framework for large-scale gradient-based design optimization of high-performance structures. *Finite Elements in Analysis and Design*.

[5] Cesnik, C. E. S. and Brown, E. L. (2005). Modelling of High Aspect Ratio Active Flexible Wings for Roll Control.

[6] Shearer, C. M. and Cesnik, C. E. S. (2007). Nonlinear Flight Dynamics of Very Flexible Aircraft. *Journal of Aircraft*, 44(5), 1528–1545. ISSN 0021-8669. doi:10.2514/1.27606.

[7] Su, W. and Cesnik, C. E. S. (2010). Nonlinear Aeroelasticity of a Very Flexible Blended-Wing-Body Aircraft. *Journal of Aircraft*, 47(5), 1539–1553. ISSN 0021-8669. doi: 10.2514/1.47317.

[8] A. Peters, D. and J. Johnson, M. (1994). Finite-state airloads for deformable airfoils on fixed and rotating wings. 44, 1–28.

[9] Skujins, T. (2012). *Reduced-Order Modeling of Unsteady Aerodynamics Across Multiple Mach Regimes*. Ph.D. thesis, Ann Arbor, MI.

[10] Teixeira, P. C. and Cesnik, C. E. S. (2017). Inclusion of Propeller Effects on Aeroelastic Behavior of Very Flexible Aircraft. In *IFASD*. Como, Italy, pp. 1–18.

[11] Teixeira, P. C. and Cesnik, C. E. S. (2018). Propeller effects on the dynamic response of HALE aircraft. In *AIAA/ASCE/AHS/ASC Structures, Structural Dynamics, and Materials Conference*. Kissimee, FL. ISBN 9781624105326. doi:10.2514/6.2018-1202.

[12] Lupp, C. A. and Cesnik, C. E. S. (2019). A Gradient-Based Flutter Constraint Including Geometrically Nonlinear Deformations. In *SciTech*. San Diego, CA: AIAA.

[13] Jonsson, E., Riso, C., Lupp, C. A., et al. (In Press). Flutter and post-flutter constraints in aircraft design optimization. *Progress in Aerospace Sciences*.

[14] Jonsson, E., Mader, C. A., Kennedy, G. J., et al. (2019). Computational Modeling of Flutter Constraint for High-Fidelity Aerostructural Optimization. In *59th AIAA Structures, Structural Dynamics, and Materials Conference*. San Diego, California.

[15] Sanghi, D. and Censik, C. E. S. (2018). Enhanced fem2stick formulation. Tech. rep.

[16] Stodieck, O., Cooper, J. E., Neild, S. A., et al. (2018). Slender-Wing Beam Reduction Method for Gradient-Based Aeroelastic Design Optimization AIAA JOURNAL, 1–17. ISSN 0001-1452. doi:10.2514/1.J056952.

[17] Sagebaum, M., Albring, T., and Gauger, N. R. (2017). High-Performance Derivative Computations using CoDiPack. *arXiv preprint arXiv:1709.07229*.

[18] Brooks, T. R., Kenway, G. K. W., and Martins, J. R. R. A. (2018). Benchmark aerostructural models for the study of transonic aircraft wings. *AIAA Journal*, 56, 2840––2855. doi:DOI: 10.2514/1.J056603. ¡p¿All the files for the models in this paper are ¡a href=”http://mdolab.engin.umich.edu/ucrm”¿available on the uCRM page¡/a¿.¡/p¿.

COPYRIGHT STATEMENT